

Anisotropic Quantum Annealing vs Trit Annealing

M. Haider Akbar^{1,*} and Özgür E. Müstecaplıoğlu^{2,3,†}

¹*Department of Computational Sciences and Engineering,
Koç University, 34450 Sarıyer, İstanbul, Türkiye*

²*Department of Physics, Koç University, 34450 Sarıyer, İstanbul, Türkiye*

³*TÜBİTAK Research Institute for Fundamental Sciences, 41470 Gebze, Türkiye*

(Dated: December 30, 2025)

Quantum annealing offers a promising strategy for solving complex optimization problems by encoding the solution into the ground state of a problem Hamiltonian. While most implementations rely on spin-1/2 systems, we explore the performance of quantum annealing on a spin-1 system where the problem Hamiltonian includes a single ion anisotropy term of the form $D \sum_i (S_i^z)^2$. Our results reveal that for a suitable range of the anisotropy strength D , the spin-1 annealer reaches the ground state with higher fidelity. We attribute this performance to the presence of the intermediate spin level and the tunable anisotropy, which together enable the algorithm to traverse the energy landscape through smaller, incremental steps instead of a single large spin flip. This mechanism effectively lowers barriers in the configuration space and stabilizes the evolution. These findings suggest that higher spin annealers offer intrinsic advantages for robust and flexible quantum optimization, especially for problems naturally formulated with ternary decision variables.

I. INTRODUCTION

Combinatorial optimization arises across physics, computer science, and engineering, with applications from materials and circuit design to logistics, portfolio optimization, and scheduling [1, 2]. Many such problems can be cast as minimizing a cost function over discrete variables, naturally mapping to the ground state of an effective Ising-type Hamiltonian with local fields and pairwise couplings [3–7]. Candidate solutions correspond to spin configurations, while optimal or near-optimal solutions lie at low energies. Since the configuration space grows exponentially with system size, classical methods can struggle on rugged, frustrated landscapes with many nearly degenerate local minima.

Quantum annealing (QA) is a heuristic approach to such optimization problems that leverages quantum fluctuations [4, 5, 8]. The protocol initializes the system in the ground state of a simple driver Hamiltonian—typically a transverse field term that does not commute with the problem Hamiltonian—and then interpolates toward the problem Hamiltonian under a time-dependent schedule. In the coherent, adiabatic limit, the system follows the instantaneous ground state provided the evolution is sufficiently slow. In practice, the runtime is constrained by the minimum spectral gap encountered along the annealing path [5, 8, 9]; small gaps therefore require long schedules and increase susceptibility to non-adiabatic excitations, decoherence, and control errors [10].

Most theoretical and experimental QA platforms use effective spin-1/2 degrees of freedom (qubits), which directly encode binary decision variables [6, 8, 11–14]. However, many practically relevant optimization problems are intrinsically multivalued, motivating approaches

that go beyond binary encoding. Examples include ternary decisions (e.g., buy/hold/sell) and formulations with variables taking values in sets such as $\{-1, 0, +1\}$. On qubit based architectures, representing multivalued logic typically requires embedding each variable into multiple qubits together with penalty terms enforcing logical constraints [2]. These embeddings increase hardware overhead, reduce effective connectivity, and complicate the energy landscape, potentially shrinking relevant gaps and amplifying sensitivity to noise and control imperfections. Higher spin systems provide a natural alternative in which multilevel quantum degrees of freedom directly encode multivalued variables.

Spin-1 systems, in particular, have three eigenstates of S^z labeled by $m_s = -1, 0, +1$, enabling a direct representation of ternary variables without elaborate embeddings. This has motivated interest in multilevel quantum optimization and in understanding how extra levels affect adiabatic protocols [2, 10, 15, 16]. Beyond compact encoding, spin-1 models also introduce control parameters absent in spin-1/2 systems. A key example is the single ion anisotropy term $D \sum_i (S_i^z)^2$, familiar from spin-1 magnetism such as the Blume–Capel model [17, 18], which tunes the relative energetics of the $m_s = 0$ and $m_s = \pm 1$ states. Since $(S^z)^2$ is proportional to the identity for spin-1/2, this anisotropy provides a genuine additional control knob for spin-1 annealers and gives rise to richer behavior along the annealing path.

The remainder of this paper is organized as follows. We introduce the spin-1 annealing Hamiltonian and trit based simulated annealing in Sec. II. Sec. III describes our numerical protocol and performance metrics. In Sec. IV, we compare the spin-1 annealer with classical annealing. Sec. V summarizes our findings and outlines directions for future work. Physical interpretations based on the structure of the classical energy landscape are discussed in Appendix A.

* makbar25@ku.edu.tr

† omustecap@ku.edu.tr

II. THEORETICAL FRAMEWORK

We consider a spin-1 quantum annealer, encoding each trit in the local S^z eigenbasis $\{|+1\rangle, |0\rangle, |-1\rangle\}$, satisfying

$$S^z|m_z\rangle = m_z|m_z\rangle, \quad m_z \in \{-1, 0, +1\}. \quad (1)$$

In this basis, the spin operators are

$$S^z = \begin{pmatrix} 1 & 0 & 0 \\ 0 & 0 & 0 \\ 0 & 0 & -1 \end{pmatrix}, \quad S^x = \frac{1}{\sqrt{2}} \begin{pmatrix} 0 & 1 & 0 \\ 1 & 0 & 1 \\ 0 & 1 & 0 \end{pmatrix}, \quad (2)$$

with $[S^\alpha, S^\beta] = i\epsilon_{\alpha\beta\gamma}S^\gamma$. The system evolves under the time-dependent Hamiltonian

$$H(t) = H_P + H_D(t), \quad (3)$$

where the problem Hamiltonian is

$$H_P = -J \sum_{\langle i,j \rangle} S_i^z S_j^z - h \sum_i S_i^z + D \sum_i (S_i^z)^2, \quad (4)$$

and the driver Hamiltonian is

$$H_D(t) = -g(t) \sum_i S_i^x. \quad (5)$$

Here S_i^α are spin-1 operators acting on site i , and the parameters are defined as

- J is the coupling constant that determines the interaction strength between adjacent spins,
- h is the longitudinal field, representing an external field that creates an energy preference for spin alignment in the z direction,
- D is the single ion anisotropy parameter,
- $g(t)$ is the annealing schedule controlling the strength of the transverse field.

By construction, H_P is the quantum embedding of the classical cost function: on computational basis states $|s_1, \dots, s_N\rangle$ with $S_i^z|s_i\rangle = s_i|s_i\rangle$ and $s_i \in \{-1, 0, +1\}$, one has

$$H_P|s_1, \dots, s_N\rangle = H(s)|s_1, \dots, s_N\rangle. \quad (6)$$

Let $\{|\psi_k(t)\rangle, E_k(t)\}$ be the instantaneous spectrum of $H(t)$ with ground state $k=0$. The adiabatic bound [9] gives

$$1 - P_{gs} \lesssim \max_t \frac{|\langle\psi_1(t)|\dot{H}(t)|\psi_0(t)\rangle|^2}{\Delta(t)^4}, \quad (7)$$

with gap $\Delta(t) = E_1(t) - E_0(t)$. Near an avoided crossing with minimum gap Δ_{\min} , a two level linearization yields the Landau-Zener formula [19]

$$P_{\text{exc}} \approx \exp\left(-\frac{\pi\Delta_{\min}^2}{2\hbar|\alpha|}\right), \quad (8)$$

where α is the diabatic slope difference.

The corresponding classical configuration space is

$$\mathcal{S} = \{-1, 0, +1\}^N, \quad (9)$$

with cost function

$$H(s) = -J \sum_{\langle i,j \rangle} s_i s_j - h \sum_{i=1}^N s_i + D \sum_{i=1}^N s_i^2. \quad (10)$$

At temperature $T > 0$, a single-site Metropolis update [20] proceeds as follows:

1. Pick a site $i \in \{1, \dots, N\}$ uniformly at random.
2. Propose a new local value $s'_i \in \{-1, 0, +1\} \setminus \{s_i\}$ uniformly over the two alternatives (the proposal distribution is symmetric).
3. Let s' be s with s_i replaced by s'_i . Define the local energy for setting $s_i = m$ by

$$\varepsilon_i(m) = -Jm \sum_{j \in \partial i} s_j - hm + Dm^2, \quad (11)$$

where ∂i denotes the neighbors of i . The associated energy change is

$$\Delta E = H(s') - H(s) \quad (12)$$

$$= \varepsilon_i(s'_i) - \varepsilon_i(s_i) \quad (13)$$

$$= -(s'_i - s_i) \left(J \sum_{j \in \partial i} s_j + h \right) + D[(s'_i)^2 - s_i^2]. \quad (14)$$

4. Accept the proposal with Metropolis probability

$$P_{\text{acc}}(s \rightarrow s') = \min \left\{ 1, e^{-\Delta E/T} \right\}; \quad (15)$$

otherwise keep s .

III. METHODS

We compare anisotropic quantum annealing (AQA) with trit annealing (TA) on a one dimensional nearest neighbor open chain of length $N = 5$. Each site carries a spin-1 degree of freedom, giving a Hilbert space dimension $\dim \mathcal{H} = 3^N$, which remains small enough to allow exact diagonalization of the problem Hamiltonian and numerically controlled evolution. To lift the degeneracy between globally spin flipped configurations while preserving the essential competition between exchange and single-ion anisotropy, we fix the longitudinal field to a small nonzero value $h = 0.2$. This symmetry breaking field selects a unique classical ground state for each (J, D) pair but is sufficiently weak not to qualitatively alter the underlying physics. Working at fixed small N

lets us disentangle intrinsic algorithmic behavior from finite size scaling issues, while the resulting spectrum still exhibits nontrivial features such as avoided crossings and associated diabatic effects.

Both AQA and TA are driven by annealing schedules that share the same overall shape, specified by a smooth function of a dimensionless time parameter. In AQA, the system evolves under a time dependent Hamiltonian $H(t)$ that goes from a transverse driver to classical problem Hamiltonian via a scalar control function $g(t)$ over a total evolution time T . In TA, we use the same functional form to define a cooling schedule, but now parameterized over a total of S Monte Carlo sweeps, so that the classical dynamics experiences an analogous slowdown pattern. The transverse driver amplitude is scheduled as

$$g(t) = \frac{e}{f(t)}, \quad e \in \{1, 5, 10, 20\}, \quad (16)$$

with four representative decay profiles

$$f(t) \in \left\{ \log(1+t), \sqrt{t}, t, t^2 \right\}. \quad (17)$$

For AQA we numerically integrate the Schrödinger equation for the time dependent Hamiltonian $H(t)$ using a fourth order Suzuki Trotter factorization [21] with time step δt . At each step we decompose $H(t)$ into sums of non commuting local terms and apply the corresponding product of short-time evolution operators. Convergence of the Trotterized evolution is verified by systematically halving δt until changes in all observables of interest become negligible. In particular, we require that Trotter errors be much smaller than the diabatic losses expected from the instantaneous gap and transition matrix elements entering Eqs. (7)–(8) in the theoretical framework, so that any observed deviation from perfect ground state preparation can be attributed to genuine nonadiabatic effects rather than numerical artifacts. The initial state is taken to be the exact ground state of the driver Hamiltonian, and the state $|\psi(T)\rangle$ at the end of the evolution is obtained. Quantum annealing performance is quantified by the ground state fidelity

$$P_{AQA} = |\langle \psi_g | \psi(T) \rangle|^2, \quad (18)$$

where $|\psi_g\rangle$ is the exact ground state of the problem Hamiltonian.

TA is defined on the same set of spin configurations by taking the classical cost function to be the diagonal of the quantum problem Hamiltonian, so that classical and quantum instances are exactly aligned at the level of their energy landscapes. One sweep comprises N single site updates, in which each spin is updated once on average according to the local Boltzmann weights at the current effective temperature. The inverse temperature is reduced following the same schedule shape $g(t)$ used in the quantum protocol, now applied over the course of S sweeps. For each disorder instance (coupling realization) we perform R independent TA runs starting from random

initial spin configurations drawn uniformly from the 3^N classical states. At the end of each run (r) we record the terminal energy $E_{\text{final}}^{(r)}$. The exact classical ground state energy E_0 is obtained by exhaustive enumeration of all configurations. We define the TA success probability as

$$P_{\text{TA}} = \frac{1}{R} \sum_{r=1}^R \mathbb{I} \left[|E_{\text{final}}^{(r)} - E_0| \leq 10^{-6} \right], \quad (19)$$

where $\mathbb{I}[\cdot]$ denotes the indicator function. The small numerical tolerance accounts for floating point round off while effectively requiring that the algorithm reaches the true ground state. By matching instance sets, schedule shapes, and problem Hamiltonians between AQA and TA, we can directly compare their success probabilities.

IV. RESULTS

Figure 1 compares the performance of AQA and TA across the (J, D) plane for all transverse field scales and schedules considered. The dominant trends are governed by the driver strength e , the anisotropy sector (easy-plane $D > 0$ versus easy-axis $D < 0$), and the late-time decay of the schedule $g(t)$.

For weak driving ($e = 1$, top row), TA is comparable to AQA over nearly the entire parameter range, as indicated by the predominance of blue regions across all schedules. In this regime, the transverse field contribution is insufficient, within the fixed runtime, to reliably generate transitions that improve the final success probability. The sparse red features occur in narrow parameter bands near boundaries between distinct classical ordering tendencies, consistent with cases where near degeneracies permit limited benefit from coherent mixing.

As the driver strength increases ($e = 5$ and above), extended parameter regions emerge in which AQA outperforms TA. This advantage is most apparent in the easy-plane sector ($D > 0$) at intermediate coupling magnitudes $|J|$, where red domains become substantial for $e = 5$ and expand further for $e = 10$ and $e = 20$. The growth of these AQA favorable regions indicates that sufficiently strong transverse driving can more effectively exploit low energy structure associated with competing classical patterns.

The easy-axis sector ($D < 0$) exhibits a more restrained AQA advantage. Across many parameters TA remains competitive, and broad AQA dominant regions occur less frequently than in the easy-plane case. This behavior is consistent with an effective restriction of relevant low energy configurations to the ± 1 -subspace when the 0-level is disfavored, which reduces the diversity of low energy pathways available to intermediate state dynamics (See App. A for more details).

Across all driver strengths, structured V-shaped and X-shaped patterns appear near order change boundaries. These boundary regions are frequently associated with

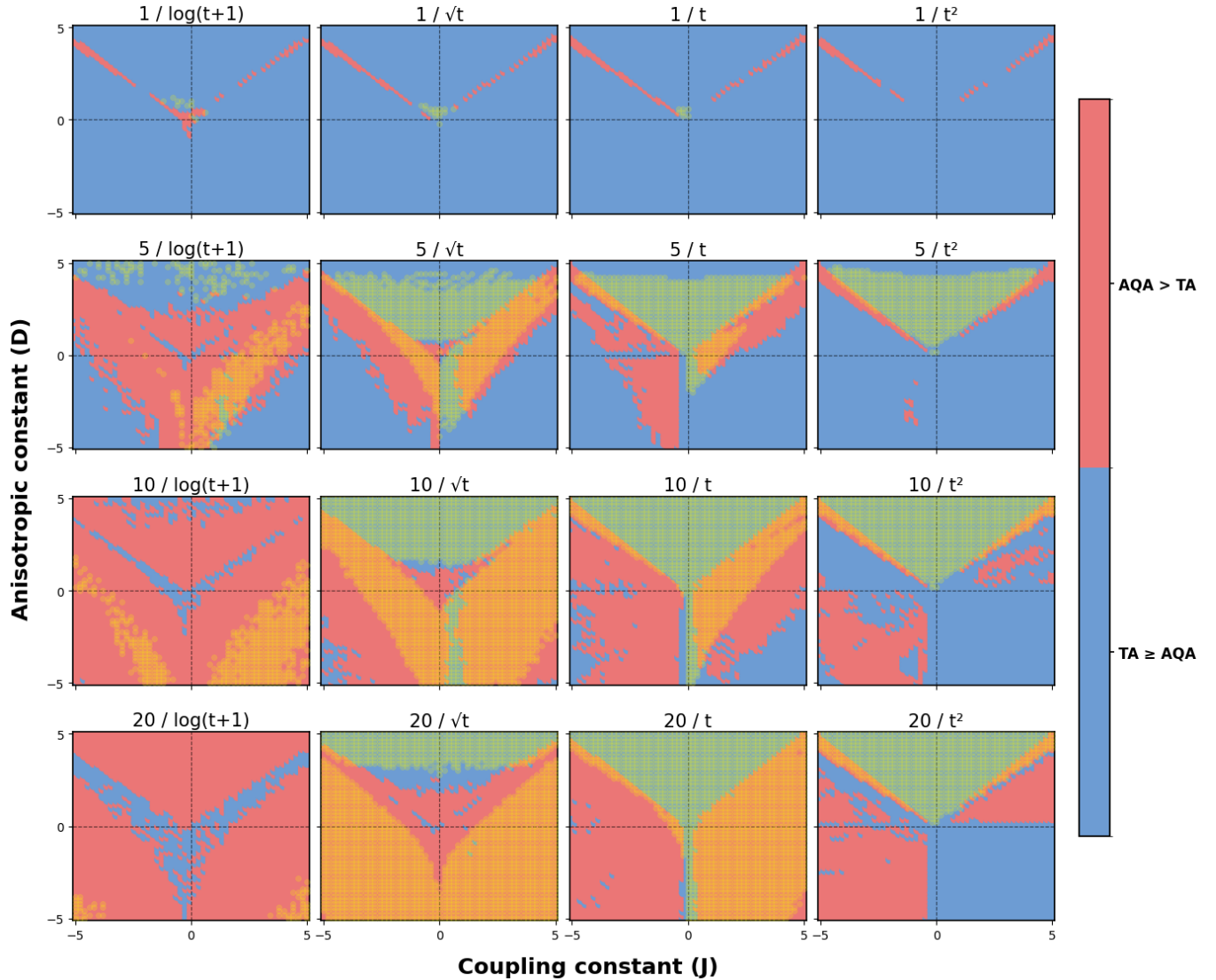


FIG. 1. AQA versus TA across the coupling–anisotropy plane. Each panel displays the difference $P_{\text{AQA}} - P_{\text{TA}}$ over the (J, D) plane for a fixed transverse field scale e and annealing schedule $g(t)$, at longitudinal field $h = 0.2$. Columns (left to right) correspond to schedules with late-time decay $g(t) \propto 1/\log(1+t)$, $1/\sqrt{t}$, $1/t$, and $1/t^2$, while rows (top to bottom) correspond to $e = 1, 5, 10, 20$. Red (blue) indicates parameter regions where AQA yields higher (lower) success probability than TA, and yellow markers indicate cases with $P_{\text{AQA}} > 0.9$. The dashed gray lines at $J = 0$ and $D = 0$ delineate the easy-plane ($D > 0$) and easy-axis ($D < 0$) sectors and assist in identifying symmetry-related structures.

reduced performance for both protocols, producing narrow corridors in which the relative advantage alternates and separating neighboring domains with more uniform behavior.

At fixed e , performance exhibits a systematic dependence on the schedule. Slower late-time decays expand the parameter regions where AQA outperforms TA, with the effect most pronounced at larger e . In contrast, faster decays yield comparatively larger regions where TA remains dominant. These observations are consistent with the view that, at fixed total runtime, emphasizing late-time evolution enhances AQA’s ability to resolve and traverse competing low-energy structures.

V. CONCLUSION

This study investigated quantum and classical annealing dynamics for an open boundary spin-1 Ising chain with quadratic anisotropy. Across the (J, D) plane, we observed a consistent pattern: quantum advantage emerges when two conditions are jointly satisfied, namely (i) a sufficiently delocalized initial state (large e) and (ii) schedules that allocate more time at small g . In these regimes, especially near order-change ridges where the dominant pattern shifts (all-0, all- ± 1 , antiferromagnetic), the dynamics benefit from stepwise rearrangements rather than a single collective switch. This dis-

tributes the evolution over multiple avoided crossings and can improve adiabatic transport relative to schedules that effectively force a single collective switch.

A second, schedule dependent effect concerns how the annealing time is distributed between the driver dominated and problem dominated parts of the evolution. For decays that naturally dwell near the final Hamiltonian (e.g., $g(t) \propto 1/\log(1+t)$) and at larger e , we observe systematically larger regions in which AQA outperforms TA, indicating that additional late-time budget is crucial for resolving competition between low energy patterns once the transverse field is weak. Linear ramps, by contrast, retain sizable TA dominant patches even at $e=20$, underscoring that the terminal slowdown is an operational rather than purely cosmetic feature. Overall, TA performance follows the structure of classical barriers, while AQA shows additional sensitivity to schedule shape and transverse scale, consistent with coherent pathways that circumvent the need for collective flips (see App. A for supporting classical landscape diagnostics).

All comparisons use matched time budgets and identical $g(t)$ grids, so the observed advantage is a finite time effect under controlled conditions rather than an asymptotic separation. The present study nevertheless considers a single chain with open boundary condition, a fixed symmetry breaking field h , and one classical baseline. Future comparisons against additional classical heuristics (e.g., simulated annealing with optimized temperature schedules, population annealing, or cluster updates adapted to ternary variables) would strengthen the baseline. Likewise, scaling with system size and alternative graph topologies (rings, weak disorder, or sparse long-range couplings) will be important to assess robustness. Finally, schedule design itself is a practical lever: local adiabatic ramps, explicit end pauses, or counter-diabatic corrections could sharpen the quantum protocol without

altering the problem Hamiltonian.

To the best of our knowledge, this is one of the first detailed investigations of ternary optimization within a quantum annealing framework using a spin-1 system with a quadratic anisotropy. We find evidence for a narrow but reproducible region in the (J, D) plane where quantum systems outperform classical systems under matched finite time budgets. The advantage becomes most visible when the initial transverse scale e is large and the schedule allocates sufficient time at small g , conditions that jointly promote coherent transport across sequences of avoided crossings near order-change boundaries, particularly in the easy-plane sector ($D > 0$). Conversely, with insufficient driving or an aggressive terminal ramp, AQA can underperform even on classically easy instances.

These findings point to a pragmatic strategy for multi valued optimization: shape the problem's local structure, particularly through the D term, to open coherent pathways, and employ schedules that prioritize the endgame of the evolution. A more definitive characterization of the quantum classical performance boundary will require comprehensive spectral and landscape diagnostics, additional observables such as entanglement and participation ratios, and broader baselines and system sizes. Taken together, the present results and these next steps outline a concrete path toward establishing when and how spin-1 quantum annealing can provide a meaningful advantage in ternary optimization settings.

ACKNOWLEDGMENTS

We thank Seyda Leyla Bozan for suggesting useful and relevant references.

[1] Stella L. Harrison, Helgi Sigurdsson, Sergey Alyatkin, Julian D. Töpfer, and Pavlos G. Lagoudakis, “Solving the max-3-cut problem with coherent networks,” *Physical Review Applied* **17**, 024063 (2022).

[2] Jordi R. Weggemans, Alexander Urech, Alexander Rausch, Robert Spreeuw, Richard Boucherie, Florian Schreck, Kareljan Schoutens, Jiří Minář, and Florian Speelman, “Solving correlation clustering with QAOA and a Rydberg qudit system: a full-stack approach,” *Quantum* **6**, 687 (2022).

[3] A. B. Finnila, M. A. Gomez, C. Sebenik, C. Stenson, and J. D. Doll, “Quantum annealing: A new method for minimizing multidimensional functions,” *Chemical Physics Letters* **219**, 343–348 (1994).

[4] Tadashi Kadowaki and Hidetoshi Nishimori, “Quantum annealing in the transverse ising model,” *Phys. Rev. E* **58**, 5355–5363 (1998).

[5] Andrew M. Childs, Edward Farhi, and John Preskill, “Robustness of adiabatic quantum computation,” *Phys. Rev. A* **65**, 012322 (2001).

[6] Arnab Das and Bikas K. Chakrabarti, “Colloquium: Quantum annealing and analog quantum computation,” *Rev. Mod. Phys.* **80**, 1061–1081 (2008).

[7] Andrew Lucas, “Ising formulations of many NP problems,” *Frontiers in Physics* **2**, 5 (2014).

[8] Tameem Albash and Daniel A. Lidar, “Adiabatic quantum computation,” *Rev. Mod. Phys.* **90**, 015002 (2018).

[9] Sabine Jansen, Mary-Beth Ruskai, and Ruedi Seiler, “Bounds for the adiabatic approximation with applications to quantum computation,” *Journal of Mathematical Physics* **48**, 102111 (2007).

[10] Alberto Bottarelli, Mikel Garcia de Andoin, Pranav Chandarana, Koushik Paul, Xi Chen, Mikel Sanz, and Philipp Hauke, “Symmetry-enhanced counterdiabatic quantum algorithm for qudits,” *Physical Review Research* **7**, 043030 (2025).

[11] P. Hauke, H. G. Katzgraber, W. Lechner, H. Nishimori, and W. D. Oliver, “Perspectives of quantum annealing: Methods and implementations,” *Reports on Progress in Physics* **83**, 054401 (2020).

- [12] M. W. Johnson, M. H. S. Amin, S. Gildert, T. Lanting, F. Hamze, N. Dickson, R. Harris, A. J. Berkley, *et al.*, “Quantum annealing with manufactured spins,” *Nature* **473**, 194–198 (2011).
- [13] Vasil S. Denchev, Sergio Boixo, Sergei V. Isakov, Nan Ding, Ryan Babbush, Vadim Smelyanskiy, John Martini, and Hartmut Neven, “What is the computational value of finite-range tunneling?” *Physical Review X* **6**, 031015 (2016).
- [14] Sergio Boixo, Vadim N. Smelyanskiy, Alireza Shabani, Sergei V. Isakov, Mark Dykman, Vasil S. Denchev, Mohammad H. Amin, Anatoly Yu. Smirnov, Masoud Mohseni, and Hartmut Neven, “Computational multi-qubit tunnelling in programmable quantum annealers,” *Nature Communications* **7**, 10327 (2016).
- [15] M. H. S. Amin, Neil G. Dickson, and Peter Smith, “Adiabatic quantum optimization with qudits,” *Quantum Information Processing* **12**, 1819–1829 (2013), arXiv:1103.1904 [quant-ph].
- [16] Yuchen Wang, Zixuan Hu, Barry C. Sanders, and Sabre Kais, “Qudits and high-dimensional quantum computing,” *Frontiers in Physics* **8**, 589504 (2020).
- [17] M. Blume, “Theory of the first-order magnetic phase change in $u\alpha_2$,” *Phys. Rev.* **141**, 517–524 (1966).
- [18] H. W. Capel, “On the possibility of first-order phase transitions in ising systems of triplet ions with zero-field splitting,” *Physica* **32**, 966–988 (1966).
- [19] Clarence Zener, “Non-adiabatic crossing of energy levels,” *Proceedings of the Royal Society of London. Series A, Containing Papers of a Mathematical and Physical Character* **137**, 696–702 (1932).
- [20] Nicholas Metropolis, Arianna W. Rosenbluth, Marshall N. Rosenbluth, Augusta H. Teller, and Edward Teller, “Equation of state calculations by fast computing machines,” *The Journal of Chemical Physics* **21**, 1087–1092 (1953).
- [21] Johann Ostmeyer, “Optimised trotter decompositions for classical and quantum computing,” *Journal of Physics A: Mathematical and Theoretical* **56**, 285303 (2023).

Appendix A: Energy Landscape Structure

This appendix provides supporting evidence for the qualitative interpretation of landscape used in the main text. As a concrete proxy for how “funnel-like” versus fragmented the classical landscape is under local updates, we (i) quantify ruggedness through a basin decomposition induced by one-step moves and (ii) visualize the distribution of one-step local minima by plotting the classical energy $H(s)$ against a simple order parameter.

We define adjacency via one-step single site moves $s_i \mapsto s_i \pm 1$ (i.e. $-1 \leftrightarrow 0 \leftrightarrow +1$). A configuration m is a one-step local minimum if none of its one-step neighbors has strictly lower energy. Starting from any configuration s , we iteratively move to a strictly lower energy one-step neighbor (using a deterministic tie-break when multiple downhill moves exist) until reaching a fixed point m . This procedure partitions the full configuration space into basins of attraction $B(m)$, indexed by their corresponding local minima m .

We report two summary statistics:

- Number of basins: the number of distinct one-step local minima.
- Largest basin fraction: $\max_m |B(m)|/3^N$, the fraction of all configurations that drain into the largest basin.

These quantities are computed by enumeration to provide a concrete, interpretable proxy for landscape ruggedness.

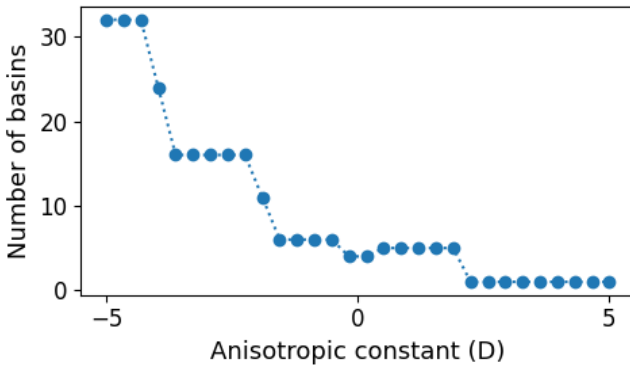


FIG. 2. Number of basins versus D along an antiferromagnetic cut ($J = -2$). Stepwise decreases reflect qualitative reorganizations of the set of minima as the anisotropy is varied.

Figures 2 and 3 quantify how the classical landscape reorganizes with D along a representative antiferromagnetic cut. For strongly negative D , many distinct local minima coexist and no single basin dominates, consistent with a rugged landscape. As D increases, the basin count drops in discrete steps while the largest basin fraction rises, indicating a progressive shift toward a more funnel-like structure. For sufficiently large positive D , the largest basin fraction approaches unity and the basin

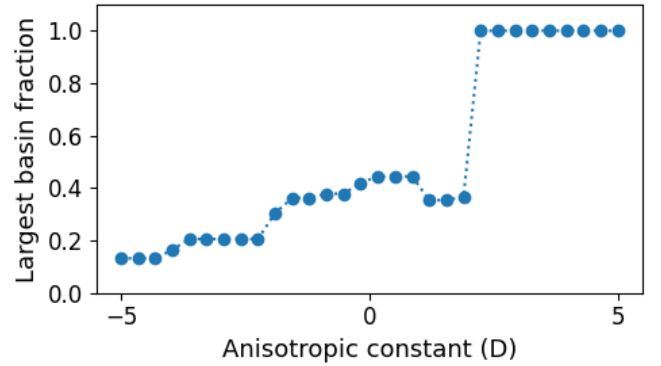


FIG. 3. Dominance of the largest basin versus D along the cut ($J = -2$). Growth of this fraction signals an increasingly funnel-like landscape; values near unity indicate that almost all configurations drain to a single minimum.

count collapses to one, consistent with a classically simple limit.

To characterize these landscapes, we introduce the fraction of sites occupying the ± 1 levels for a given classical configuration s ,

$$f(s) = \frac{1}{N} \sum_{i=1}^N \mathbf{1}_{|s_i|=1}, \quad (A1)$$

where $\mathbf{1}_{|s_i|=1} = 1$ if $s_i = \pm 1$ and 0 otherwise. Thus $f = 0$ for the all-0 configuration and $f = 1$ for configurations with no 0-spins.

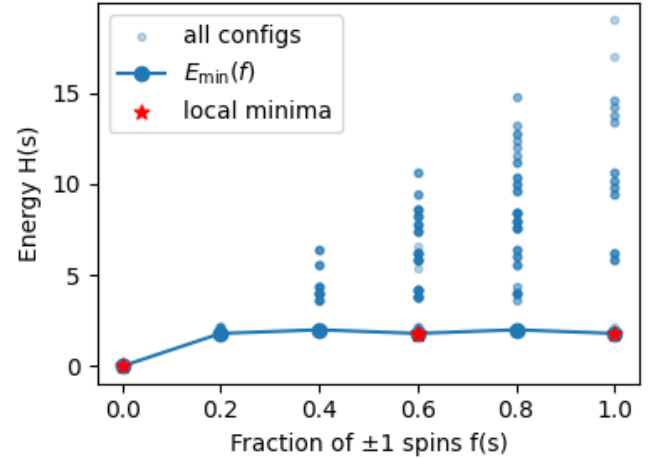


FIG. 4. Easy-plane energy landscape along an antiferromagnetic cut. Classical energy $H(s)$ versus the fraction $f(s)$ of spins in the ± 1 levels for $J = -2$ and $D = +2$. Light blue points show all configurations; the solid line indicates, for each f , the minimum energy over configurations with that f ; star markers denote one-step local minima (basin roots). The local minima separate into distinct clusters at different f , reflecting competing orders and a multi-basin structure in this order-parameter coordinate.

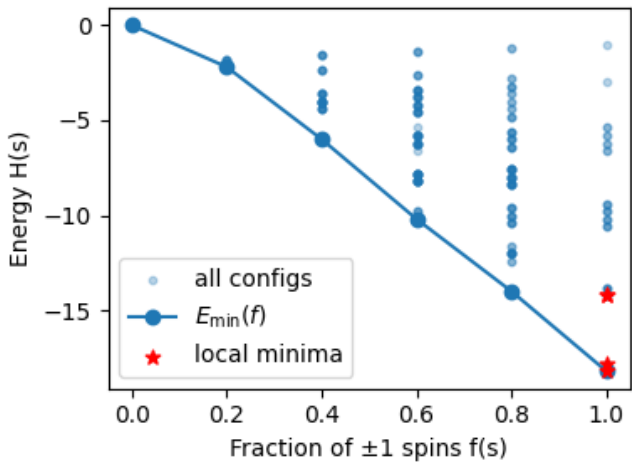


FIG. 5. **Easy-axis energy landscape along an antiferromagnetic cut.** Classical energy $H(s)$ versus fraction $f(s)$ for $J = -2$ and $D = -2$, with one-step local minima marked by stars. In contrast to the easy-plane case, low energy states and local minima concentrate near $f = 1$ and are less clearly separated in f , indicating a comparatively less partitioned structure in this coordinate.

Figures 4 and 5 visualize the distribution of one-step local minima in a physically meaningful coordinate. In the easy-plane case ($D = +2$), local minima (stars) occur in multiple well separated clusters at different f , consistent with competing orders involving both 0-rich and ± 1 -rich configurations. In the easy-axis case ($D = -2$), the low energy configurations and minima are concentrated near $f = 1$ and are less clearly separated in f , consistent with the 0-level being energetically disfavored and the low energy structure being dominated by ± 1 occupations.